



Understanding migration barriers for monovalent ion insertion in transition metal oxide and phosphate based cathode materials: A DFT study

D.A. Aksyonov^{a,*}, S.S. Fedotov^{a,b}, K.J. Stevenson^a, A. Zhugayevych^a

^a Skoltech Center for Electrochemical Energy Storage, Skolkovo Institute of Science and Technology, 143026 Moscow, Russian Federation

^b Department of Chemistry, Lomonosov Moscow State University, 119991 Moscow, Russian Federation

ARTICLE INFO

Keywords:

Li-ion
Na-ion
K-ion
Transition metal-ion cathode materials
Migration barriers
DFT calculations

ABSTRACT

High ionic conductivity is a prerequisite requirement for materials used in monovalent metal-ion rechargeable batteries. The extensive search of new electrode materials for Na-ion and K-ion monovalent metal-ion batteries requires a deep understanding of structural and chemical details of cation migration through the crystal lattice. In the paper, we consider three classes of transition metal oxide and phosphate cathode materials: AMn_2O_4 spinels, AMPO_4 olivines and AVPO_4F tavorite (A = Li, Na, K, □; M = Fe, Mn), used for pragmatic applications for secondary (rechargeable) batteries. Herein we examine Na^+ and K^+ migration characteristics in comparison with that of Li^+ by means of DFT+U, local energy calculations, empirical potentials, and bond valence energy landscape (BVEL). It is found that despite larger radii of Na^+ and K^+ , the migration barriers are comparable with that of Li^+ . In several cases, we reveal that the migration barrier of K^+ can be even lower than that of Li^+ . This behavior is explained through the interplay of site and lattice energies during cation migration. For automation of screening of migration properties via DFT calculations, a new Python-based framework (SIMAN) is developed and benchmarked across three cathode materials structures.

1. Introduction

The portable electronic device revolution and upcoming transition to all electric vehicles (EV), heavily relies on Li-ion battery technology, which has led to a doubling of the prices for Li precursors in several years [1]. As a result, the interest in the alternative potentially cheaper battery systems, such as Na-ion (NIB) and K-ion (KIB) has been reignited [2,3]. Remarkably, owing to the negligible contribution of Li to the mass and cost of Li-ion cell (~3%), the price of Li itself has little effect on the battery prices [4]. For example, the use of Al anode current collector in NIB and KIB systems can provide greater cost reductions [2]. A more convincing reason to study alternative chemistries is the highly uneven distribution of Li across the continents [5]. Looking ahead, the worldwide transition to EV would exhaust the seemingly plentiful global terrestrial lithium reserves, even with the extensive recycling, not to mention the battery demand for larger scale needs such as grid storage [6]. Probably the most motivating reason to develop NIB and KIB relies upon the highly variable chemistries above known and better understood LIBs crystal structures, which provides great impetus to outperform Li-ion systems especially in grid-scale applications. However, this requires discovery of new cathode, anode, and electrolyte materials, as the existing NIB and KIB are usually more

limited than LIBs, including the most decisive parameter, such as cost per Watt-hour [2].

One emerging and promising approach for materials discovery is to develop high throughput computational screening methods with respect to identifying specific properties [7]. One of such properties, essential for battery materials, is high ionic conductivity of charge carrier ions. However, the direct calculation of conductivity for example with density functional theory (DFT) is fairly complicated, hindering its usage in high-throughput screening. Therefore various models based on descriptors that correlate with barriers have been developed [8]. To improve the predictive power of such models it is important to understand the underlying physics of the diffusion process at the atomic level.

The influence of chemical composition and crystal structure on the diffusion process was systematically studied with DFT methods [9–11]. Leaving aside the statistical nature of the diffusion phenomena, the essential parameter that determines diffusion coefficient is activation energy (migration barrier) required for an atom to hop from one lattice site to another. The following features of the atomic structure were found to determine the migration barrier: (i) a number of vacancies involved in the atomic hops (layered oxides and sulfates) [12,13]; (ii) change of lattice constants due to cation extraction (layered materials) [14]; (iii) change of the transition metal (TM) oxidation state due

* Corresponding author.

E-mail address: d.aksenov@skoltech.ru (D.A. Aksyonov).

to cation extraction [15]; (iv) Jahn–Teller distortion corresponding to the TM state through the change of the distance between the adjacent O ions (LiTi₂O₄ example) [16,17]. The mentioned effects are responsible for concentration dependence of the cation diffusion coefficient.

In addition to the mentioned factors, it is highly tempting to establish a quantitative relationship between migration barrier and local atomic structure for the given chemical composition. The simplest geometrical approach based on the open space metrics proved to be of limited use, mainly for a preliminary tentative analysis, while more reliable chemistry-related methods are still being developed [18]. It is hard to judge whether the same factors affect migration barriers for Li⁺, Na⁺ and K⁺ cations. The comparison of Li⁺ and Na⁺ diffusion in layered and olivine structures was done by Ong et al. [19], by whom it was found that the migration barriers for Na⁺ can be lower in layered structure but higher in olivine structure, than that for Li. Only few studies of cation migration were done for K. It is still not clear whether the migration barriers for K⁺ should be larger than that for Li⁺ and Na⁺. One of the most appropriate tools to solve this problem is DFT that provides detailed information on the deformation of the local atomic structure during migration, as well as relaxation effects and charge redistribution.

In the current work, we study the migration of cations in cathode materials using DFT, extending it to Na and K containing materials. As a straightforward approach, we consider several most efficient Li-ion cathode materials belonging to oxide (LiMn₂O₄), phosphate (LiMPO₄), and fluoride-phosphate (LiVPO₄F) classes and their Na- and K-substituted structural analogues taking into account that an electrochemical exchange of Li⁺ by Na⁺/K⁺ is widely adopted as an efficient approach in the experimental design of new cathodes [20,21]. Since this approach usually results in stabilizing metastable structures, it gives a unique opportunity to compare the influence of cation size in the equivalent crystal structures. In addition to that, we calculate migration barriers of Na and K in thermodynamically stable structures.

Considering several different crystal structures in two concentrations (initial and deintercalated states) and for three cations requires performing hundreds of DFT calculations. To maximize the efficiency and reduce time-costs we employed our custom-developed package SIMAN for automation of the DFT calculations, which is first-time introduced in this paper.

In Sections 2 and 3 we present calculation details and developed package SIMAN, respectively. In Section 4 we report crystal and electronic structures of considered compounds as well as intercalation voltages and volumes for Li, Na, and K. In Section 5 we present migration barriers calculated with DFT/DFT+U and discuss their correlation with different geometry and energy descriptors. The conclusions are provided in the final section.

2. Computational methodology

All DFT calculations are performed in VASP program [22] using generalized gradient approximation (GGA) to exchange-correlation functional and standard PAW PBE potentials [23] with minimum number of valence electrons. Tetrahedron method with Blöchl corrections is used for Brillouin-zone integrations [24]. The energy cut-off is fixed at 400 eV, the k-point density is between 0.2 and 0.3 Å⁻¹. The DFT+U calculations are carried out using Dudarev scheme [25]. The values of U are the same as in the work of Jain et al. [26]: 4, 3.9, and 3.1 eV for Fe, Mn, and V, respectively. To improve the wave-function convergence the U-ramping approach is employed [27].

To eliminate Pulay errors the lattice optimization (ISIF = 4) is performed at constant volume for several contracted and expanded cells (7 points). The size of the supercell used in calculations of ion-diffusion barriers is about 10 Å, corresponding to one hundred atoms on average. The maximum force permitted for any vector component is 0.02 eV/Å except for KVPO₄F and KMnPO₄ with K vacancies, where the maximum forces are 0.2 eV/Å and 0.17 eV/Å.

The migration barriers are determined using nudged elastic band (NEB) method as implemented in VASP. The method allows to find minimum energy path, which includes several intermediate configurations (images) between initial and final states. Since, the geometry of pathways in the considered materials is simple, only three intermediate images are used.

In addition to DFT-NEB, accessible pathways for mobile ions in the structure and migration barriers have been estimated with Bond valence energy landscape (BVEL) methodology. It is based on the empirically established relationships between the bond length, R , and the so-called bond valence, V defined by the formula [28]

$$V_{A-X} = \exp\left(\frac{R-R_0}{b}\right), \quad (1)$$

where R_0 and b are tabulated constants. Regions of a structure, where the BV sum, $V(A) = \sum V_{A-X}$, over all adjacent counter-ions X is close to the “ideal valence”, $V_{id}(A)$, or in other words the absolute value of its oxidation state (1 in case of Li, Na and K), are considered suitable for migration of Li⁺, Na⁺ and K⁺. To convert the BV values into the site energy, $E(A)$, a Morse-type interaction potential is used. For BVEL calculations we use the 3DBVSMAPPER program, which generates a spatial distribution of $E(A)$ energy values within the entire unit cell [29]. The resulting three-dimensional grid can be adjusted by the activation energy parameter [E_{act} , i.e. the difference between the cut-off value of $E(A)$ and minimum $E(A)$, E_{min}] to locate and visualize the most energetically favorable areas for a particular ion. The minimum E_{act} value required for the areas to merge into a continuous system can be considered as an energy barrier within this approach.

The average intercalation voltages are calculated according to the following equation (on the example of LiMn₂O₄):

$$\bar{V} = \frac{E(\text{Li}_{x1}\text{Mn}_2\text{O}_4) - E(\text{Li}_{x2}\text{Mn}_2\text{O}_4) - (x1 - x2)E(\text{Li})}{x1 - x2}, \quad (2)$$

where $E(\text{Li}_x\text{Mn}_2\text{O}_4)$ is the full energy of the supercell with x Li atoms and $E(\text{Li})$ is the energy of bcc-Li per atom. The average potential and volume changes are calculated for $x1 = 1$ and $x2 = 0$. All DFT calculations are performed using a specially developed SIMAN package, described in the next section.

3. Python package SIMAN

To process large number of similar DFT calculations we developed a management package SIMAN, written in Python programming language. The primary goal of SIMAN is to provide a platform for smart generation of input for DFT codes, such as VASP, batch submission of jobs, and extraction of output results in concise, ready for analysis form on the local computer. Thus, each calculation is represented as a special object, which is persistently stored in the database dictionary. For convenient addressing of the database a special naming convention is proposed. The key of each calculation should consist of three elements: the name of the atomic structure, the name of parameters set, the version of the structure. This naming system allows for keeping identical atomic structures calculated with various parameter sets and under different conditions, straightforward comparison of different structures for the same set of parameters, and an account of deformed structures by assigning them with a unique version number.

3.1. Reading atomic structures and input parameters

The initial atomic structure can be provided from common atomic data format files:

```
1 Li = smart_structure.read('Li2bcc.cif')
```

or obtained from Materials project database [30]:

```
1 Li = get_structure_from_matproj(mat_proj_id = '
    mp-135'),
```

where `Li` is the object of internal class `Structure()` with many fields named as in the input format of the ABINIT DFT code [31]. For example, `Li.rprimd` contains primitive lattice vectors, while `Li.xcart` contains Cartesian coordinates of atoms.

A supercell can be created with the following command:

```
1 Li10 = supercell(Li, [10, 10, 10])
```

The tool creates the supercell with primitive vectors having two properties: (i) similar lengths as close to 10 Å as possible; (ii) being orthogonal or close to orthogonal.

The set of parameters is described with the special object of class `InputSet()`. For interfacing with VASP, the values of parameters could be provided explicitly as values of dictionary field `vasp_param` or read from INCAR file:

```
1 new = InputSet()
2 new.read_incar('INCAR')
```

The set can be added to the predefined persistent dictionary by

```
1 sets['S400'] = new
```

To create a new set 'S600' with a larger cut-off energy it is enough to run:

```
1 read_vasp_sets([( 'S600', 'S400', { 'ENCUT': 600 })])
```

3.2. Workflow

We illustrate the workflow by calculating the equilibrium lattice constants of the bcc Li depending on the cut-off energy. Firstly, two sets of parameters 'S400' and 'S600' are created. Secondly, the file with the initial atomic structure is placed in the folder with the chosen name of the structure (say 'Li2bcc'). After that it is enough to run

```
1 add('Li2bcc', ['S400', 'S600'], 1, run = 1,
    calc_method = 'uniform_scale')
```

Alternatively, the atomic structure could be provided as a `Structure()` object using the `input_st` argument. The command implements several actions: (i) scale initial structure (by default in the range from -4% to +4% by seven images); (ii) prepare all necessary files such as POSCAR, INCAR, KPOINTS, and run scripts for both parameters sets; (iii) copy everything to a default cluster (multiple clusters with different queue systems are supported); (iv) submit job; (v) create `Calculation()` objects with atomic and supporting data. The created objects of `Calculation()` class are available in the database dictionary `db`, which supports persistence and can be saved on the file system using the pickle serialization format with `write_database()` command. Reading of the database is achieved with the `read_database()` command, which is invoked in the beginning of the script. By running the following two commands:

```
1 db['Li2bcc.su', 'S400', 1].init.printme()
2 db['Li2bcc.su', 'S400', 1].set.printme()
```

the atomic data and calculation parameters will be shown for the particular calculation. After completion of the calculations the results can be obtained by running:

```
1 res('Li2bcc', ['S400', 'S600'],
    [1,2,3,4,5,6,7,100], analys_type = 'fit_a')
```

The command downloads OUTCAR files for each set and each scaled version. The version No. 100 contains a crystal structure with optimized

lattice constants, which were obtained automatically on the cluster with additional tool `fit_tool.py`. Finally, the OUTCARs are analyzed, the most important information, including energies, lattice constants, convergence is printed on the screen in a concise form as well as a figure with volume-energy plot with fit to one of the equations of state is showed and saved in the file system. The `res()` checks the consistency of calculation with respect to several criteria, and provides additional information by using `show` argument.

3.3. Calculation sequences

The sequence of calculations with the transfer of the output atomic structure is also possible. For example, to make a two-step relaxation using conjugate-gradient and quasi-Newton algorithms followed by a single point static run the following actions should be performed. First, three corresponding sets 'CG', 'QN', and 'SP' are created. Then they are combined in one sequence set 'seq':

```
1 read_vasp_sets([( 'seq', 'CG', { 'set_sequence'
    : [ 'QN', 'SP' ] })])
```

After that the command

```
1 add('Li2bcc', 'seq', 1)
```

will prepare all input files, including the bash script for three sequential VASP runs with transmission of optimized atomic structure between the runs and zipping of output files.

3.4. U-ramping method

In the spin-polarized case, the electronic energy surface in the spin space may contain numerous local minima. Therefore, simple algorithms for obtaining self-consistent field may not guarantee the convergence to the ground-state. The situation is worsened in the case of the DFT+U approach, in which localization of electrons adds additional degrees of freedom, and determination of the ground state becomes a challenge. Meredig et al. suggested a method for locating low energy solutions by a gradual increase of the *U* value and iterative application of previous orbital occupation matrices [27]. In the VASP program these matrices can be applied by using the previous wave function and charge density. The authors suggested ramping *U* by a small value of 0.1 eV until all bands are integrally occupied. The method is implemented in the SIMAN package. To employ it, a special set should be created:

```
1 read_vasp_sets([( 'S400ur10', 'S400', {
    'u_ramping_nstep': 10 })])
```

where required number of steps (10) is provided. By running `add()` function with 'S400ur10' set, the special batch script is produced. In the script the *U* values of transition metal atoms are gradually increased from 0 to the final value in 10 steps, while the atomic structure, and occupation matrices are transferred to the each subsequent run.

3.5. Intercalation potentials

The intercalation potential can be obtained from the total energies of cathode material with different cation concentrations. On the example of Na₂FePO₄F, which contains two symmetry nonequivalent positions of Na, the initial atomic structure of the deintercalated NaFePO₄F compound can be created as

```
1 st = smart_structure_read(input_geo_file = 'in/
    Na2FePO4F.POSCAR')
2 st1 = create_deintercalated_structure(st, 'Na',
    del_pos = 1)
```

where `del_pos` provides the nonequivalent position from which Na

atoms are removed. To remove all atoms:

```
1 stDS = st.remove_atoms(['Na'])
```

After corresponding `add` and `res` commands, the intercalation potential and volume are calculated using

```
1 calc_redox(db['Na2FePO4F', 's400', 1], db['NaFePO4F', 's400', 1]).
```

3.6. Migration barriers

The migration barriers for the diffusion are calculated using the NEB method, as implemented in VASP. The procedure that requires identifying relevant migration paths, optimization of initial and final configurations, followed by optimization of intermediate images with NEB method is implemented in SIMAN. The initial and final positions of migrating atom could be chosen as lattice sites or interstitial voids, the positions of which are determined based on hard spheres approximation. To calculate the barriers the following command should be invoked:

```
1 it = add_neb(db['Na2FePO4F', 's400', 1].end, images = 3)
```

where `images` is the number of intermediate structures used for NEB calculation. After the calculation is finished the command

```
1 res(it, 's400', range(1,6), analysis = 'neb')
```

produces the energy profile plot, the minimum energy migration path and calculates the migration barrier value.

3.7. Vacancies and antisite defects

To create Na vacancy, the following wrapper command is used.

```
1 make_defect(db['Na2FePO4F', 's400', 1], 'Na', option = 'vac')
```

It produces a structure with a defect and automatically invokes the corresponding `add()` command. After the calculation is completed the command reads the results using `res()` and calculates vacancy formation energy.

The antisite defects, such as exchange of Na and Fe can be considered using the command

```
1 create_antisite_defect(db['Na2FePO4F', 's400', 1].end, 'Na', 'Fe', max_sep = 4)
```

which creates all possible unique antisite configurations based on symmetry, where `max_sep` defines the maximum separation between Na and Fe.

3.8. Charge-density differences, density of electronic and phonon states

Numerous small tools for analysis of DFT results are available in SIMAN package. The charge-density differences calculated as

```
1 cal_chg_diff(db['Na2FePO4F', 's400', 1], db['NaFePO4F', 's400', 1])
```

Assuming that a special set `'dos'` with `LORBIT = 12` is created, the partial local density of states (PDOS) can be plotted with

```
1 plot_dos(db['Na2FePO4F', 'dos', 1], db['NaFePO4F', 'dos', 1], iatom = 27, iatom2 = 20,
2         dostype = 'partial', orbitals = ['t2g', 'eg'])
```

allowing to compare t_{2g} and e_g orbitals on specific atoms in the

$\text{Na}_2\text{FePO}_4\text{F}$ and NaFePO_4F compounds.

For phonon analysis the special wrapper for PHONOPY code `read_pdos_using_phonopy()` is available.

3.9. Other functionality

The provided examples demonstrate the basic functionality. More control is available through additional parameters and methods. A part of SIMAN functionality is realized using Pymatgen [32] and Atomic Simulation Environment [33]. The detailed tutorials are provided on the project website [34].

4. Atomic and electronic structure of intercalated and deintercalated compounds

4.1. Description of chosen compounds

In this work, we study one oxide, two phosphates, and four fluorophosphates. The LiMn_2O_4 oxide has the spinel crystal structure with the $Fd\bar{3}m$ space group and Li^+ cations located in tetrahedral sites. The DFT studies confirmed that the material has 3D diffusion [35] with significant dependence of migration barriers on the oxidation state of surrounding Mn atoms [36] and Jahn-Teller (JT) distortions [37]. Due to the 3D character of diffusion and low migration barriers the material is commercialized for use in Li-ion batteries for power applications [38]. It was experimentally shown that Li^+ can be electrochemically exchanged with Na^+ in LiMn_2O_4 [20].

The considered olivine phosphate LiFePO_4 with the $Pnma$ space group is one of the most thoroughly studied cathode materials, which was successfully commercialized several years ago [39]. Numerous DFT studies of migration phenomena conducted for LiFePO_4 showed that the diffusion is 1D with low migration barriers [40–43]. It was reliably demonstrated that Li^+ can be electrochemically exchanged with Na^+ [21]. The obtained Na-based olivine is successfully cycled without transformation into electrochemically inactive maricite structure [44]. No attempts of K intercalation into the olivine structure were published. Apparently, the KFePO_4 olivine would be highly unstable and would transform upon cycling into electrochemically inactive KFePO_4 phase with the $P2_1/n$ space group [45]. In addition to LiFePO_4 we consider a similar LiMnPO_4 olivine phosphate, which is characterized by a higher intercalation voltage.

Finally, to study fluorophosphates we choose LiVPO_4F with the tavorite structure ($P\bar{1}$) [46]. In LiVPO_4F the diffusion is predominantly 1D [46]. It was shown that isostructural tavorite NaVPO_4F can be synthesized [47]. Since in the case of fluorophosphates the Na and K can form electrochemically active ground state structures, we consider two additional compounds. The $\text{Na}_2\text{FePO}_4\text{F}$ with $Pbcn$ space group described by Ellis et al. [48] is characterized by 2D diffusion with relatively low migration barriers of 0.3–0.4 eV [49,50]. The KVPO_4F with $Pna2_1$ space group, recently synthesized by Fedotov et al. [51] is empirically predicted to have a 1D migration, which is confirmed by the explicit diffusion coefficient measurements [52]. The cathode material is considered as promising for high-power applications.

4.2. Calculation of lattice constants

The initial atomic structures of the described compounds in a fully intercalated state are taken either from the materials project database [30] or from experimental studies. The structures for Na and K-containing counterparts are obtained by manually replacing Li^+ in the parent structure with Na^+ or K^+ followed by full optimization of the cell. The fully deintercalated structures are obtained by removing all alkali ions with subsequent optimization of the crystal structure.

The calculated equilibrium lattice constants in comparison to the experiment are collected in Table 1. It is seen that in almost all cases theory overestimates experiment by 1–2%, which is a well-known issue

Table 1
Lattice parameters (Å), volume (Å³) and space group (spg) of the considered structures.

Structure	Source	a	b	c	V	spg
LiMn ₂ O ₄	exp [56]	8.24	8.24	8.24	561.2	<i>Fd3m</i>
LiMn ₂ O ₄	DFT + U	8.41	8.41	8.41	593.9	<i>Fd3m</i>
Difference, %		2.06	2.06	2.06	6	
NaMn ₂ O ₄	DFT + U	8.68	8.68	8.68	654.3	<i>Fd3m</i>
KMn ₂ O ₄	DFT + U	9.13	9.13	9.13	761.5	<i>Fd3m</i>
LiFePO ₄	exp [57]	10.33	6.01	4.69	291.4	<i>Pnma</i>
LiFePO ₄	DFT + U	10.42	6.07	4.76	300.9	<i>Pnma</i>
Difference, %		0.80	1.07	1.36	3	
NaFePO ₄	DFT + U	10.56	6.25	4.99	329.3	<i>Pnma</i>
KFePO ₄	DFT + U	10.81	6.64	5.48	393.1	<i>Pnma</i>
LiMnPO ₄	exp [58]	10.42	6.09	4.73	300.1	<i>Pnma</i>
LiMnPO ₄	DFT + U	10.56	6.17	4.80	312.8	<i>Pnma</i>
Difference, %		1.35	1.38	1.45	4	
NaMnPO ₄	DFT + U	10.70	6.37	5.02	342.5	<i>Pnma</i>
KMnPO ₄	DFT + U	10.73	6.82	5.33	389.7	<i>Pnma</i>
LiVPO ₄ F	exp [59]	5.17	5.31	7.50	174.2	<i>P1</i>
LiVPO ₄ F	DFT + U	5.25	5.39	7.47	184.5	<i>P1</i>
Difference, %		1.53	1.50	-0.43	6	
NaVPO ₄ F	DFT + U	5.42	5.42	7.50	191.0	<i>P1</i>
KVPO ₄ F	DFT + U	5.64	5.50	7.55	200.9	<i>P1</i>
Li ₂ FePO ₄ F	exp [60]	10.42	6.48	10.95	739.4	<i>Pnma</i>
Li ₂ FePO ₄ F	DFT + U	10.56	6.54	11.04	762.7	<i>Pnma</i>
Difference, %		1.39	0.90	0.82	3	
Na ₂ FePO ₄ F	DFT + U	11.02	6.83	11.58	871.6	<i>Pnma</i>
K ₂ FePO ₄ F	DFT + U	12.04	7.37	12.79	1134.2	<i>Pnma</i>
KVPO ₄ F	exp [51]	12.82	6.39	10.61	870.0	<i>Pna2₁</i>
KVPO ₄ F	DFT + U	13.09	6.52	10.83	924.5	<i>Pna2₁</i>
Difference, %		2.12	2.00	2.11	6	
Na ₂ FePO ₄ F	exp [61]	5.22	13.85	11.78	851.9	<i>Pbcn</i>
Na ₂ FePO ₄ F	DFT + U	5.25	13.95	11.90	871.2	<i>Pbcn</i>
Difference, %		0.56	0.69	1.02	2	

for the GGA PBE functional [53]. We have found that the Pulay stress for the considered materials at the energy cutoff of 400 eV is in the order of -5 GPa. Since in our work we employ the constant volume procedure optimization, which results in the constant energy cutoff, the influence of the Pulay error on the lattice constants is minimal [54,55]. However, frequently the volume optimization is performed at a fixed number of plane waves, which due to the incompleteness of the basis set is more vulnerable to the Pulay error. Owing to the negative Pulay stress the lattice constants are underestimated, coincidentally compensating the PBE error. Apparently, the latter approach should be avoided.

All resulting Na and K based structures are isostructural to those of Li. However, in the case ofavorite more pronounced shape changes are observed. As it is seen from Table 1 the substitution of Li with larger cations results in a non-uniform increase of the lattice constants. Moving from Li to K the *a*, *b*, and *c* lattice constants are increasing by 7.4%, 2%, and 1%, respectively. The predominant increase of *a* affects unit cell angles and relative distances between the atoms, changing the lowest energy migration path for K.

4.3. Electronic structure

The site-projected partial density of states (PDOS) for transition metal and six nearest neighbor oxygen atoms for LiFePO₄, NaFePO₄, and KFePO₄ are shown in Fig. 1. For other compounds the PDOS plots are provided in Supplementary Information in Figs. S1–S17. By comparing PDOS for the same crystal framework with different alkali cations we observe the following trends. The distances between the peaks decrease moving from Li to Na and K, which is a direct result of the lattice expansion. The DOS of all considered Na-based compounds turned out to be similar to that of Li-based compounds in terms of peaks

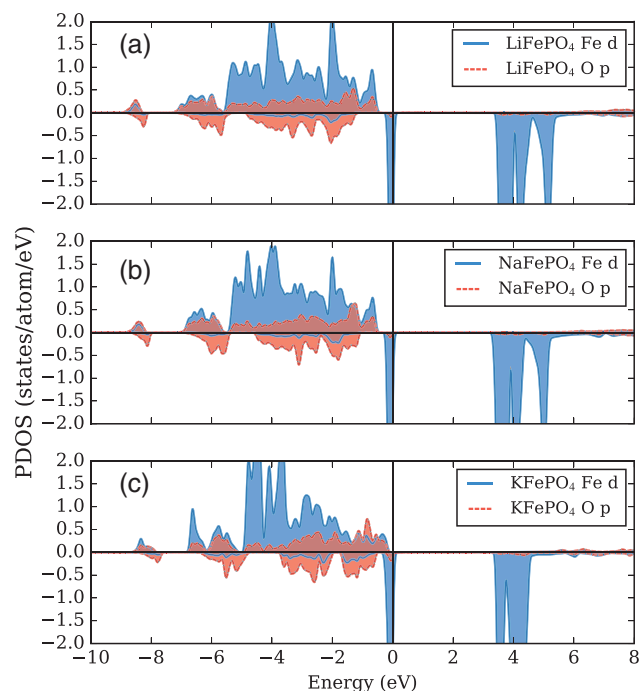


Fig. 1. Site-projected PDOS for AFePO₄ (*Pnma*). The *d* and *p* orbitals are provided for Fe and six nearest neighbor O atoms, respectively. The Fermi level is at 0 eV.

intensity and their relative positions. In contrast, more pronounced changes are observed for the K-based compounds, including the different intensities of peaks. These changes should be responsible for structure destabilization upon substitution of Na and K for Li.

4.4. Intercalation potentials and volume changes

The relative volume changes for initial and fully deintercalated structures are shown in Fig. 2. It is seen that for K based materials the changes are very large reaching 25%. For Na, the changes are smaller but still quite noticeable (10–15%). For Li, they are in the order of 5%. The most versatile material is theavorite-type AVPO₄F, which shows only moderate volume changes for Na and K compared to Li.

The comparison of intercalation voltages for several cathode structures depending on the alkali ion is shown in Fig. 3 and in Tables S1 and S2. For all structures the voltage reduces from Li to Na and to K. However, for different structures the degree of reduction is variable: it is relatively low for theavorites, moderate for olivines and extremely

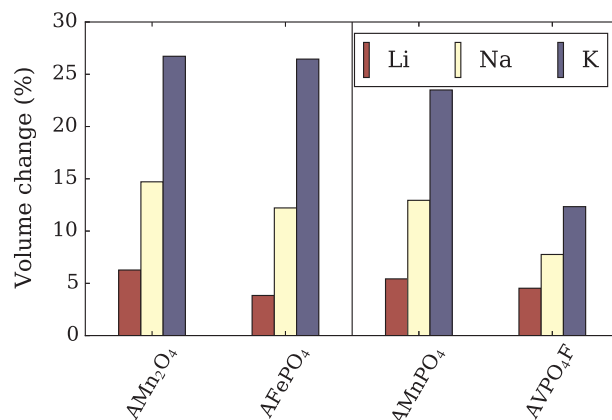


Fig. 2. The relative volume change upon deintercalation for Li, Na, and K based cathode materials calculated by DFT + U.

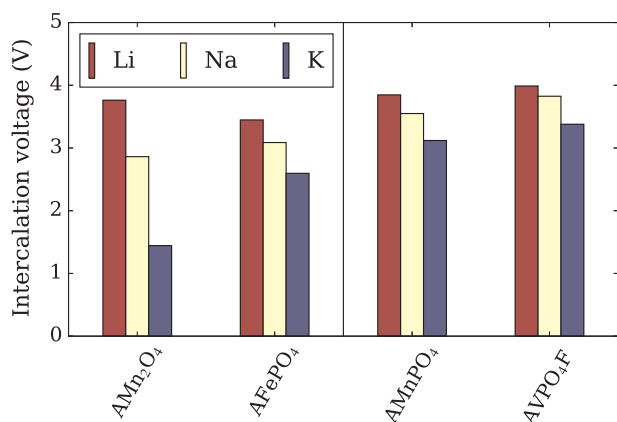


Fig. 3. Intercalation voltages for Li, Na and K based cathode compounds calculated with Eq. (2) using DFT + U results.

high for spinels AMn₂O₄. The analysis of the electronic structure for the K based tavorite shows that its PDOS is very close to that of the ground state KVPO₄F (*Pna2₁*) crystal structure (Figs. S12 and S16).

5. Migration of alkali cations

5.1. Considered paths

For the spinel, olivine and tavorite structures we consider only the shortest migration paths between alkali cation sites. It is well known that such paths have the lowest migration barriers, making them relevant for diffusion [36,40,46]. The topology of the paths is shown in Fig. 4. In the case of AFePO₄ and AMnPO₄, the initial and final positions are located in distorted oxygen octahedra. The migration occurs through two triangular faces of the octahedron. In the middle of the path, the cation is located in the tetrahedral site. The two triangles are tilted with respect to each other, the optimized path is curved. In the AMn₂O₄ structure, the initial and final positions are located in the tetrahedral sites, while migration occurs through the octahedral site and two parallel triangles. The optimized path is almost straight. A common feature of these two types of topology is highly symmetric geometry: the cation is positioned equidistantly to several anions. A more complicated topology is found in the tavorite AVPO₄F structure. The initial position of Li can be characterized as an oblique pyramid with one F atom in the base vertex. For Na and K the void resembles a distorted anticube. Along the migration path the cation moves between two oxygen pairs and one fluorine pair. The line connecting oxygen atoms in the first pair is perpendicular to the migration line with equal A-O1 and A-O2 distances during cation migration. The lines connecting the second oxygen pair and fluorine pair are tilted relative to the migration line. As a result, during migration, the cation is moving away from one anion of the pair and approach the other anion of the pair. For K, due to the pronounced distortion of the initial lattice structure the topology of the shortest migration path is slightly different. K moves

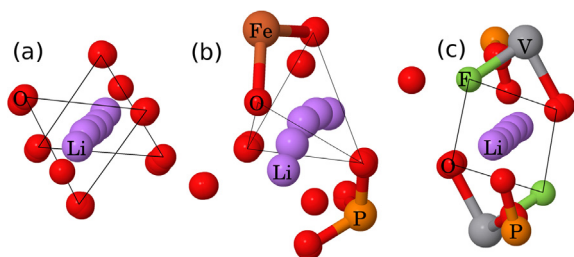


Fig. 4. The topology of considered migration paths for three classes of crystal structures: (a) spinel, (b) olivine, and (c) tavorite.

between one oxygen pair and one fluorine pair, which are tilted relative to the migration line.

For Na₂FePO₄F (*Pbcn*) and KVPO₄F (*Pna2₁*) we considered six and four relevant migration paths, respectively. We found that in these materials the lowest barrier is also achieved for the shortest migration path. Here, we provide only the lowest value of the barrier for the intercalated structures, while more details are published in our recent papers [50,62].

5.2. Barriers for Li, Na, K in intercalated and deintercalated states

In general the conductivity of carrier such as vacancy or interstitial is determined by its activation energy, which consists of formation and migration energies. The formation energy is especially important if the carrier is thermally activated. However, for the considered case of cathode materials, which work as a part of electrochemical system, the majority of carriers have athermal nature due to electrochemical activation. For dominant concentration of athermal carriers the activation energy will include only the migration barrier [63]. Therefore, in this section we consider only migration barrier. The potentials required for formation of Li vacancies and interstitials are collected in Tables S1 and S2.

The calculated values of barriers for DFT + U and DFT are shown in Figs. 5 and 6, respectively. The corresponding energy profiles are collected in Fig. S18. The influence of U on the migration barriers depends on the compound. The migration barriers for Li⁺ and Na⁺ in FePO₄ obtained with DFT + U are lower than those without U due to the vacancy/cation-small polaron interactions. A much larger barrier in NaMn₂O₄ obtained with DFT + U is the result of high-energy state found for the initial and final positions of migration path. The employment of U-ramping and occupation matrix control methods does not improve convergence of the wave function for this particular case.

The counter-intuitive result is that the values of barriers for diffusion of larger cations, Na⁺ and K⁺, do not necessary exceed those for Li⁺. In olivine, the barriers for Li⁺ and Na⁺ are comparable in both intercalated and deintercalated states, while for larger K⁺ the very low barrier of 0.1 eV is found in KFePO₄. In tavorite, the barriers for Na and K are much larger than that for Li. The lower barrier for K than that for Na in intercalated state is due to the distortion of the lattice and change of the lowest energy migration path. The migration barrier of K for the same path as for Li and Na is 1.8 eV. In the case of spinel the barriers for Na and K are comparable to that of Li, however, the saddle points are different. For Na the saddle point is located between tetrahedral and octahedral voids (Fig. S18). For K the saddle point is located in tetrahedral void, confirming that KMn₂O₄ is highly unstable.

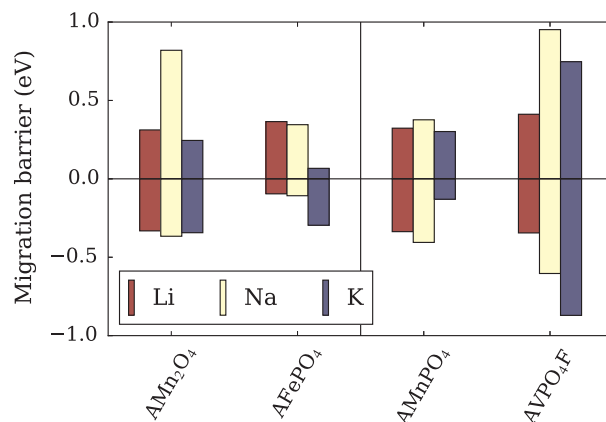


Fig. 5. Comparison of migration barriers for Li⁺, Na⁺, and K⁺ calculated using nudged elastic band method with DFT + U level of theory. The positive and negative values correspond to fully intercalated and fully deintercalated states, respectively.

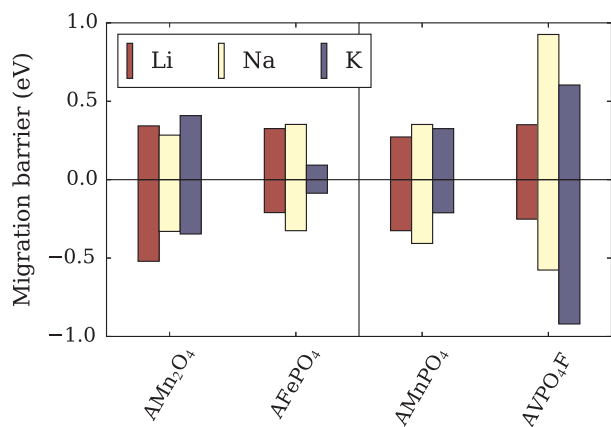


Fig. 6. Comparison of migration barriers for Li^+ , Na^+ , and K^+ calculated using nudged elastic band method with the DFT level of theory. The positive and negative values correspond to fully intercalated and fully deintercalated states, respectively.

5.3. Migration barriers for stable Na-based and K-based structures

Up to now, the discussion of Na and K migration barriers was provided for metastable crystal structures. Here, we additionally calculate migration barriers for three stable compounds: NaFePO_4 (maricite),

$\text{Na}_2\text{FePO}_4\text{F}$ (*Pbcn*), and KVPO_4F (*Pna21*). We provide only quantitative comparison of values, while a more detailed description is published in our recent papers [50,62]. Our results confirm that the migration barrier for Na in NaFePO_4 maricite is 2 eV, which explains its electrochemical inactivity. On the contrary, in $\text{Na}_2\text{FePO}_4\text{F}$ (*Pbcn*) the lowest calculated migration barrier is only 0.3 eV, which is in agreement with the previous DFT study of Tripathi et al. [49] making it an attractive cathode material for Na-ion batteries. For KVPO_4F (*Pna21*) the barrier for K vacancy migration is less than 0.2 eV, which makes it promising for high-power applications. Therefore, low migration barriers are possible not only in metastable structures, but in stable structures as well.

5.4. Descriptors of migration barriers

In this section, we test several simple models for predicting migration barriers, which are based on open space metrics, Coulomb and repulsive site energies, empirical potentials, and the BVEL method, described in Section 2. Though, the open space metrics proved to be an insufficient descriptor for a set of Li-based cathode materials [18], it is still interesting to test it for Na- and K-based cases. The employment of model site energies was successful for explaining the origin of the Li^+ migration barrier in the rutile TiO_2 [64] and spinel LiMn_2O_4 [35]. Recently, Zimmermann et al. showed that electrostatic estimation of barriers can be helpful in identifying materials with high ionic mobility

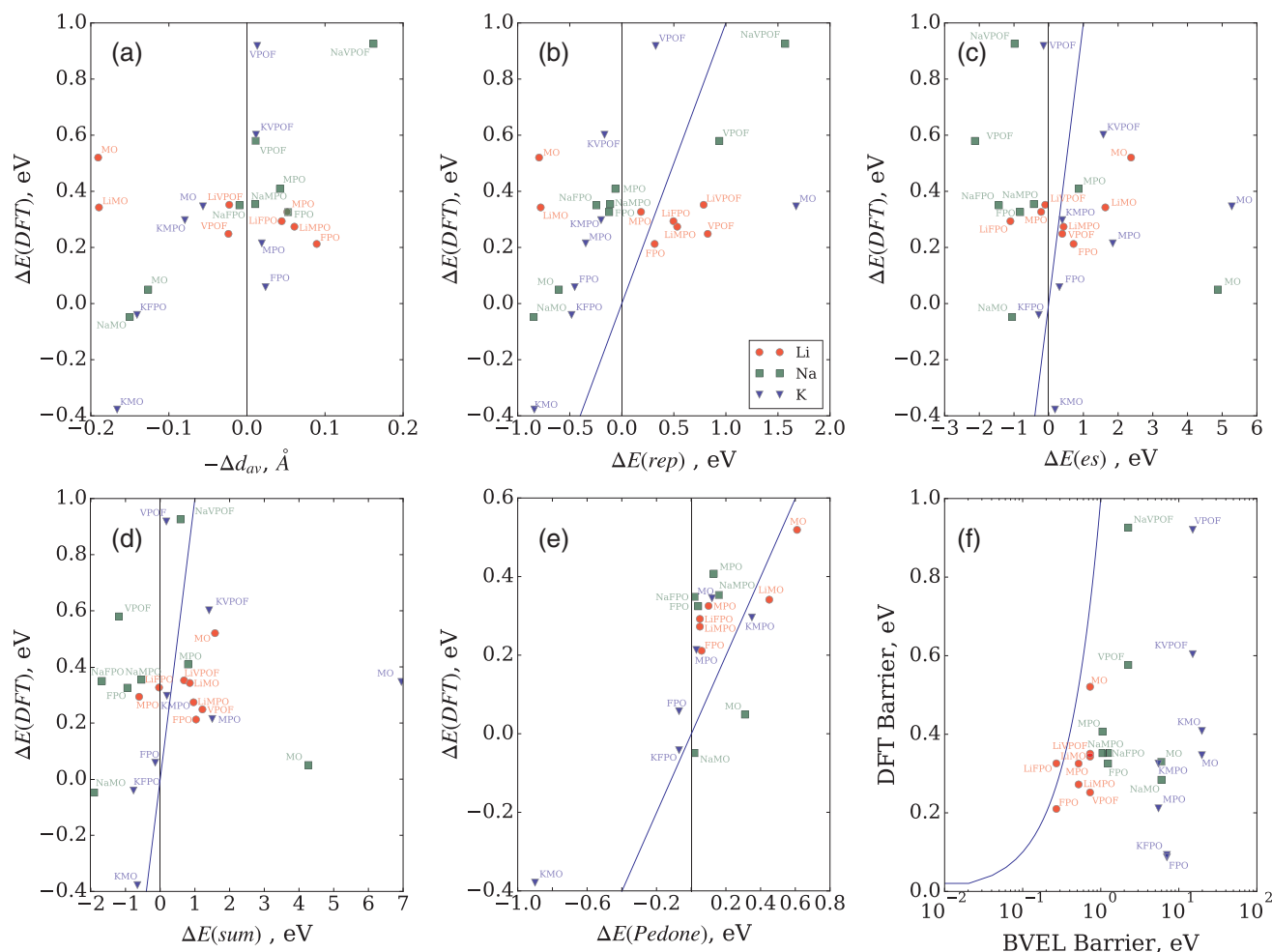


Fig. 7. Several descriptors vs DFT energy differences and barriers for alkali cation in the middle and initial positions along the migration path (a)–(e): (a) average A–(O, F) distance for four neighbors; (b) site repulsion energy; (c) site electrostatic energy; (d) sum of repulsion and electrostatic energy; (e) energy, calculated with Pedone potentials. BVEL vs DFT migration barriers are shown in (f). The solid line $x = y$ helps to see deviations from DFT results. MO = Mn_2O_4 , FPO = FePO_4 , MPO = MnPO_4 , VPOF = VPO_4F .

[65]. The bond valence methods (including bond valence energy landscapes, BVLE method) established themselves as reliable tools for fast and preliminary probing of diffusion pathways and estimating cation migration barriers, whose results corroborate well with experimentally measured electrochemical activity of cathode materials [66–68,52,69].

To validate our models, instead of migration barriers, we consider difference of energies, identically defined for all models:

$$\Delta E(\text{model}) = E^m - E^i, \quad (3)$$

where E^m and E^i are the total energies of the supercell with the alkali cation in the middle and initial positions on migration path, respectively. The comparison of $\Delta E(\text{model})$ and $\Delta E(\text{DFT})$ allows to estimate the ability of particular model to reproduce the DFT results. The reproduction of $\Delta E(\text{DFT})$ confirms that the model is able to reproduce migration barriers as well. To avoid the uncertainty due to different localization of small polarons in the DFT+U calculations, we use DFT-without-U as a reference method in this Section. All considered descriptors are calculated with a DFT-relaxed geometry for both E^m and E^i .

As open-space metric descriptor we employ the change of average A-X distance, calculated in analogy to $\Delta E(\text{model})$:

$$\Delta d_{av} = d_{av}^m - d_{av}^i, \quad (4)$$

where d_{av}^m and d_{av}^i are the average A-X distances determined by four nearest neighbors in the middle and initial positions, respectively. The obtained correspondence of Δd_{av} , Δd_{model} , and $\Delta E(\text{model})$ with $\Delta E(\text{DFT})$ as well as BVLE barriers with DFT barriers are shown in Fig. 7(a)–(f).

6. Discussion

The analysis of Fig. 7(a) shows that Δd_{av} and $\Delta E(\text{DFT})$ have poor correlation. The insufficient predictive power of average A-(O, F) distance can be attributed to the long-range nature of electrostatic interaction. To overcome this issue we explicitly calculated the Coulomb and short-range repulsive energies of the migrating cation. The Coulomb energy is calculated using the Ewald summation with ion charges determined from the Bader analysis. The repulsive energy is calculated using the Gilbert parametrization with parameters based on vibrational and crystallographic data [70]. Though the employment of Bader charges is impractical, it provides more accurate estimation of the electrostatic energy compared to that obtained with formal oxidation states of the elements. The use of Coulomb energy is justified by the fact that in the considered compounds, the alkali cations form predominantly ionic bonds with the surrounding ions [71].

The changes of the repulsive energy $\Delta E(\text{rep})$, electrostatic energy $\Delta E(\text{es})$, and their sum $\Delta E(\text{sum})$ versus $\Delta E(\text{DFT})$ are shown in Fig. 7(b–d). It is seen that $\Delta E(\text{sum})$ does not have good correlation with the DFT data either; the coefficient of determination R^2 for all points is close to zero. The obtained results based on the average distance and site energy emphasize poor predictive power of the local descriptors. Apparently, the surrounding lattice has considerable influence on the magnitude of migration barrier. This is caused by both deformation of the lattice and redistribution of the electronic density during cation migration.

An alternative way to take into account changes of the lattice energy compared to DFT is to use classical interatomic potentials. Here we employ potentials developed by Pedone et al. for oxides of Li, Na, K, P, Fe, and Mn elements [72]. It should be noted that the potentials were not specifically parametrized for the considered compounds. As it is seen from Fig. 7(e), the overall correlation is improved having $R^2 = 0.6$, while for Li R^2 exceeds 0.8. More importantly, the calculated $\Delta E(\text{Pedone})$ values are much closer to the DFT values, confirming that the account of lattice energy is equally important for accurate prediction of migration barriers.

Quantitatively, the change of lattice energy $\Delta E(\text{lat})$ can be defined

as the difference between $\Delta E(\text{Pedone/DFT})$ and $\Delta E(\text{sum})$. From Fig. 7(d, e) it can be seen that the sign and magnitude of the site and lattice contributions vary for different lattice types. For Na in Mn_2O_4 , the $\Delta E(\text{sum})$ is 4 eV, while $\Delta E(\text{Pedone})$ is only 0.3 eV, realized for highly negative $\Delta E(\text{lat})$ of -3.7 eV. For K in KFePO_4 , the $\Delta E(\text{sum})$ of -0.4 eV corresponds to $\Delta E(\text{Pedone})$ of 0 eV, realized for small positive $\Delta E(\text{lat})$ of 0.4 eV. It is seen that compensation of lattice and site energies is especially pronounced in spinel oxide structures, which results in poor correspondence between $\Delta E(\text{sum})$ and $\Delta E(\text{Pedone/DFT})$. It will be interesting to check whether this is the feature of oxide materials only, since for three polyanionic compounds the contribution of lattice energy is much smaller. If this is the case, the local site energy could be reconsidered as a descriptor for preliminary screening of cation conductivity in polyanionic compounds. By excluding AMn_2O_4 and AMn_2O_4 data points the easily calculated $\Delta E(\text{rep})$ shows improved correspondence with $\Delta E(\text{DFT})$, especially for Na and K-based cases, where the barriers change in a wider range than that for Li-based cases.

As a last step, we evaluate the correspondence between the migration barriers calculated with BVLE and DFT, shown in Fig. 7(f). It should be noted that estimation of migration barriers with BVLE is restricted by the static nature of the model, in which the relaxation of the surrounding atoms during migration is not taken into account. Since the relaxation would release local stress and subsequently lower the total energy, the BVLE migration barriers are generally higher than the computationally or experimentally obtained values. Indeed, it can be seen from Fig. 7(f) that deviation from DFT is increasing for larger cations and deintercalated structures. Omitting the Mn_2O_4 structures with a large compensative effect from the lattice, the BVLE barriers for Li, Na and K qualitatively follow the DFT results. The method is indeed useful for distinguishing materials with low and high mobility or for a tentative preliminary analysis of the key diffusion pathways, though its accuracy might be not sufficient for quantitative estimates.

Despite poor predictive power of $\Delta E(\text{sum})$, it enables better understanding of the physical origin of migration barriers. We use it to identify the reason for small migration barriers of larger cations, such as Na^+ and K^+ . For example, in olivine structures the deformation of surrounding lattice (defined through the shifts of atoms) and corresponding lattice energy is increasing in the $\text{Li}^+ \rightarrow \text{Na}^+ \rightarrow \text{K}^+$ sequence. However, both Na and K have a negative $\Delta E(\text{sum})$ contributions, compensating an increase of lattice energy (Fig. 7(d)) and resulting in barriers comparable with those of the small Li^+ cation. In KFePO_4 the compensation of lattice energy with $\Delta E(\text{sum})$ is especially effective leading to a very small barrier of 0.1 eV. In the case of KMnPO_4 , despite the same crystal structure, the compensation is less efficient. This can be due to slightly different lattice constants. According to Table 1 the a and c lattice constants of KMnPO_4 are smaller by 1%, while the b lattice constant is larger by 3%. Such change of interatomic distances violates the subtle balance between site and lattice energy contributions increasing the migration barrier.

As for theavorite structures, it can be seen that the compensation of contributions is even less efficient resulting in larger $\Delta E(\text{DFT})$ for Na and K. We ascribe it to fluorine anion, which significantly affects both site repulsive and electrostatic interactions.

7. Conclusion

Using Python programming language the package SIMAN for automation of DFT and DFT+U calculations is developed. The package simplifies determination of equilibrium lattice constants, average intercalation potentials, migration barriers and other characteristics in a batch regime.

By employing the SIMAN package several efficient Li-ion cathode materials, such as spinel LiMn_2O_4 , olivine LiFePO_4 , LiMnPO_4 , andavorite LiVPO_4F , are considered from a perspective of replacing Li^+ by Na^+ and K^+ ions. The substitution of Li^+ with Na^+ and K^+ leads to the expansion of the lattice, which is more pronounced for spinel and

olivine structures, and smaller for favorite structure. The intercalation potential upon substitution is reduced for Na^+ and K^+ , which is consistent with the reduced stability of the resulted lattices, initially optimal for small Li^+ ion. The reduction of potential is significant for spinel, moderate for olivine, and relatively small for favorite (only by 0.16 V lower for Na^+).

Comparison of the migration barriers shows that in the olivine and spinel structures the barriers for Na are comparable to those for Li. Surprisingly, in the metastable KFePO_4 the barrier for K vacancy migration is just 0.1 eV – smaller than that for the Li vacancy in LiFePO_4 (0.3 eV). In the stable KVPO_4 (*Pna2₁*) the barrier is only 0.2 eV, which corroborates well with the experimental data on the diffusion properties [52].

The calculated values of migration barriers are rationalized through the interplay of three contributions including the nearest-neighbor steric repulsion, Coulomb site energy, and lattice energy. The balance between these contributions depends on the lattice type and migrating cation. On the one hand, we find that for accurate prediction of migration barriers it is equally important to take into account both the site and lattice energies. On the other hand, low migration barriers of larger cations in the olivine structure result mainly from the smaller site energies in the saddle point. The interplay of the mentioned factors in a compensative way makes possible the existence of zero-barrier (<0.05 eV) crystal structures.

8. CRediT authorship contribution statement

D.A. Aksyonov: Conceptualization, Data curation, Formal analysis, Investigation, Methodology, Software, Visualization, Writing – original draft, Writing – review & editing. **S.S. Fedotov:** Data curation; Formal analysis; Writing – review & editing. **K.J. Stevenson:** Funding acquisition, Resources, Validation, Writing – review & editing. **A. Zhugayevych:** Data curation; Formal analysis; Resources, Supervision, Validation, Writing – review & editing.

Acknowledgments

D. Aksyonov and S. Fedotov acknowledge support from Russian Foundation for Basic Research, No. 18-33-00821. K. Stevenson and A. Zhugayevych acknowledge support from Skoltech-MIT Next Generation Program.

Appendix A. Supplementary material

Supplementary data associated with this article can be found, in the online version, at <https://doi.org/10.1016/j.commatsci.2018.07.057>.

References

- [1] G. Martin, L. Rentsch, M. Höck, M. Bertau, *Energy Storage Mater.* 6 (2017) 171.
- [2] J.W. Choi, D. Aurbach, *Nat. Rev. Mater.* 1 (2016) 16013.
- [3] J.C. Pramudita, D. Sehwat, D. Goonetilleke, N. Sharma, *Adv. Energy Mater.* (2017) 1602911.
- [4] R.E. Ciez, J.F. Whitacre, *J. Power Sources* 320 (2016) 310.
- [5] E.A. Olivetti, G. Ceder, G.G. Gaustad, X. Fu, *Joule* 1 (2017) 229.
- [6] B.A. Sand'en, P. Wallgren, *Systems Perspectives on Electromobility 2014*, Chalmers University of Technology, Goteborg, 2014.
- [7] A. Jain, Y. Shin, K.A. Persson, *Nat. Rev. Mater.* 1 (2016) 15004.
- [8] A.D. Sendek, Q. Yang, E.D. Cubuk, K.-A.N. Duerloo, Y. Cui, E.J. Reed, *Energy Environ. Sci.* 10 (2017) 306.
- [9] A. Van Der Ven, J. Bhattacharya, A.A. Belak, *Acc. Chem. Res.* 46 (2013) 1216.
- [10] M.S. Islam, C.A.J. Fisher, *Chem. Soc. Rev.* 43 (2014) 185.
- [11] Z. Rong, R. Malik, P. Canepa, G. Sai Gautam, M. Liu, A. Jain, K. Persson, G. Ceder, *Chem. Mater.* 27 (2015) 6016.
- [12] A. Van der Ven, G. Ceder, *Electrochem. Solid-State Lett.* 3 (2000) 301.
- [13] J. Bhattachar ya, A. Van Der Ven, *Phys. Rev. B* 83 (2011) 1.
- [14] K. Kang, G. Ceder, *Phys. Rev. B* 74 (2006) 1.
- [15] A. Van der Ven, G. Ceder, M. Asta, P.D. Tepesch, *Phys. Rev. B* 64 (2001) 184307.
- [16] W.J.H. Borghols, D. Lutzenkirchen-Hecht, U. Haake, E.R.H. van Eck, F.M. Mulder, M. Wagemaker, *Phys. Chem. Chem. Phys.* 11 (2009) 5742.
- [17] A.A. Belak, Y. Wang, A. Van Der Ven, *Chem. Mater.* 24 (2012) 2894.

- [18] C.J. Moore, *emph Ab initio Screening of Lithium Diffusion Rates in Transition Metal Oxide Cathodes for Lithium Ion Batteries* (Ph.D. thesis), 2012.
- [19] S.P. Ong, V.L. Chevrier, G. Hautier, A. Jain, C. Moore, S. Kim, X. Ma, G. Ceder, *Energy Environ. Sci.* 4 (2011) 3680.
- [20] N. Yabuuchi, M. Yano, S. Kuze, S. Komaba, *Electrochim. Acta* 82 (2012) 296.
- [21] Y. Zhu, Y. Xu, Y. Liu, C. Luo, C. Wang, *Nanoscale* 5 (2013) 780.
- [22] G. Kresse, J. Furthmüller, *Comput. Mater. Sci.* 6 (1996) 15.
- [23] J.P. Perdew, K. Burke, M. Ernzerhof, *Phys. Rev. Lett.* 77 (1996) 3865.
- [24] P.E. Blochl, O. Jepsen, O.K. Andersen, *Phys. Rev. B* 49 (1994) 16223.
- [25] S.L. Dudarev, G.A. Botton, S.Y. Savrasov, C.J. Humphreys, A.P. Sutton, *Phys. Rev. B* 57 (1998) 1505.
- [26] A. Jain, G. Hautier, C.J. Moore, S. Ping Ong, C.C. Fischer, T. Mueller, K.A. Persson, G. Ceder, *Comput. Mater. Sci.* 50 (2011) 2295.
- [27] B. Meredig, A. Thompson, H.A. Hansen, C. Wolverton, A. Van De Walle, *Phys. Rev. B* 82 (2010) 2.
- [28] I.D. Brown, *Chem. Rev.* 109 (2009) 6858.
- [29] M. Sale, M. Avdeev, *J. Appl. Crystallogr.* 45 (2012) 1054.
- [30] A. Jain, S.P. Ong, G. Hautier, W. Chen, W.D. Richards, S. Dacek, S. Cholia, D. Gunter, D. Skinner, G. Ceder, K.A. Persson, *APL Mater.* 1 (2013) 011002.
- [31] X. Gonze, J.M. Beuken, R. Caracas, F. Detraux, M. Fuchs, G.M. Rignanese, L. Sindic, M. Verstraete, G. Zerah, F. Jollet, M. Torrent, A. Roy, M. Mikami, P. Ghosez, J.Y. Raty, D.C. Allan, *Comput. Mater. Sci.* 25 (2002) 478.
- [32] S.P. Ong, W.D. Richards, A. Jain, G. Hautier, M. Kocher, S. Cholia, D. Gunter, V.L. Chevrier, K.A. Persson, G. Ceder, *Comput. Mater. Sci.* 68 (2013) 314.
- [33] A.H.L. Jacobsen, J.J. Mortensen, J. Blomqvist, I.E. Castelli, R. Christensen, M. Dulak, J. Friis, M.N. Groves, B. Hammer, C. Hargus, E.D. Hermes, P.C. Jennings, P.B. Jensen, *J. Phys.: Condens. Matter* 29 (2017) 273002.
- [34] <https://github.com/dimonaks/siman/wiki>.
- [35] M. Nakayama, M. Kaneko, M. Wakihara, *Phys. Chem. Chem. Phys.* 14 (2012) 13963.
- [36] B. Xu, S. Meng, *J. Power Sources* 195 (2010) 4971.
- [37] F. Ning, B. Xu, J. Shi, H. Su, M. Wu, G. Liu, C. Ouyang, *J. Mater. Chem. A* 5 (2017) 9618.
- [38] J.W. Fergus, *J. Power Sources* 195 (2010) 939.
- [39] K. Zaghib, A. Guerfi, P. Hovington, A. Vijh, M. Trudeau, A. Mauger, J.B. Goodenough, C.M. Julien, *J. Power Sources* 232 (2013) 357.
- [40] T. Maxisch, F. Zhou, G. Ceder, *Phys. Rev. B – Condens. Matter Mater. Phys.* 73 (2006) 1.
- [41] G.K.P. Dathar, D. Sheppard, K.J. Stevenson, G. Henkelman, *Chem. Mater.* 23 (2011) 4032.
- [42] Y. Sun, X. Lu, R. Xiao, H. Li, X. Huang, *Chem. Mater.* 24 (2012) 4693.
- [43] M. Nakayama, S. Yamada, R. Jalem, T. Kasuga, *Solid State Ionics* 286 (2016) 40.
- [44] B.L. Ellis, W.R.M. Makahnouk, Y. Makimura, K. Toghill, L.F. Nazar, *Nat. Mater.* 6 (2007) 749.
- [45] O.V. Yakubovich, W. Massa, O.V. Dimitrova, *Z. Anorg. Allg. Chem.* 631 (2005) 2445.
- [46] T. Mueller, G. Hautier, a. Jain, G. Ceder, *Chem. Mater.* 23 (2011) 3854.
- [47] E. Boivin, J.-N. Chotard, T. Bamine, D. Carlier, P. Serras, V. Palomares, T. Rojo, A. Iadecola, L. Dupont, L. Bourgeois, F. Fauth, C. Masquelier, L. Croguennec, *J. Mater. Chem. A* 5 (2017) 25044.
- [48] B.L. Ellis, W.R.M. Makahnouk, W.N. Rowan-Weatallukuk, D.H. Ryan, L.F. Nazar, *Chem. Mater.* 22 (2010) 1059.
- [49] R. Tripathi, S.M. Wood, M.S. Islam, L.F. Nazar, *Energy Environ. Sci.* 6 (2013) 2257.
- [50] I.V. Tereshchenko, D.A. Aksyonov, O.A. Drozhzhin, I.A. Presniakov, A.V. Sobolev, A. Zhugayevych, D. Striukov, K.J. Stevenson, E. Antipov, A.M. Abakumov, *J. Am. Chem. Soc.* 140 (2018) 3994.
- [51] S.S. Fedotov, N.R. Khasanova, A.S. Samarin, O.A. Drozhzhin, D. Batuk, O.M. Karakulina, J. Hadermann, A.M. Abakumov, E.V. Antipov, *Chem. Mater.* 28 (2016) 411.
- [52] V.A. Nikitina, S.S. Fedotov, S.Yu. Vassiliev, A.Sh. Samarin, N.R. Khasanova, E.V. Antipov, *J. Electrochem. Soc.* 164 (2017) A6373.
- [53] L. He, F. Liu, G. Hautier, M.J. Oliveira, M.A. Marques, F.D. Vila, J.J. Rehr, G.M. Rignanese, A. Zhou, *Phys. Rev. B* 89 (2014) 1.
- [54] M.C. Payne, M.P. Teter, D.C. Allan, T.A. Arias, J.D. Joannopoulos, *Rev. Mod. Phys.* 64 (1992) 1045.
- [55] D.A. Aksyonov, T. Hickel, J. Neugebauer, A.G. Lipnitskii, *J. Phys.: Condens. Matter* 28 (2016) 385001.
- [56] M.A. Monge, J.M. Amarilla, E. Gutierrez-Puebla, J.A. Campa, I. Rasines, *ChemPhysChem* 3 (2002) 367.
- [57] A. Padhi, K. Nanjundaswamy, J. Goodenough, *J. Electrochem. Soc.* 144 (1997) 1188.
- [58] N. Wizen, G. Behr, F. Lipps, I. Hellmann, R. Klingeler, V. Kataev, W. Loser, N. Sato, B. Buchner, *J. Cryst. Growth* 311 (2009) 1273.
- [59] J. Barker, R.K. Gover, P. Burns, A. Bryan, M.Y. Saidi, J.L. Swoyer, *J. Power Sources* 146 (2005) 516.
- [60] O.M. Karakulina, N.R. Khasanova, O.A. Drozhzhin, A.A. Tsirlin, J. Hadermann, E.V. Antipov, A.M. Abakumov, *Chem. Mater.* 28 (2016) 7578.
- [61] B.L. Ellis, W.R.M. Makahnouk, Y. Makimura, K. Toghill, L.F. Nazar, *Nat. Mater.* 6 (2007) 749.
- [62] S.S. Fedotov, A.S. Samarin, V.A. Nikitina, D.A. Aksyonov, S.A. Sokolov, A. Zhugayevych, K.J. Stevenson, N.R. Khasanova, A.M. Abakumov, E.V. Antipov, *J. Mater. Chem. A* 6 (2018) 14420.
- [63] K. Hoang, M.D. Johannes, *J. Phys.: Condens. Matter* 30 (2018) 293001.
- [64] P.I. Kinsbury, W.D. Ohlsen, O.W. Johnson, *Phys. Rev.* 175 (1968) 1099.
- [65] N.E.R. Zimmermann, D.C. Hannah, Z. Rong, M. Liu, G. Ceder, M. Haranczyk, K.A. Persson, *J. Phys. Chem. Lett.* 9 (2018) 628.

- [66] L. Lander, G. Rousse, A.M. Abakumov, M. Sougrati, G. van Tendeloo, J.-M. Tarascon, *J. Mater. Chem. A* 3 (2015) 19754.
- [67] E.V. Antipov, N.R. Khasanova, S.S. Fedotov, *IUCrJ* 2 (2015) 85.
- [68] S.S. Fedotov, A.A. Kabanov, N.A. Kabanova, V.A. Blatov, A. Zhugayevych, A.M. Abakumov, N.R. Khasanova, E.V. Antipov, *J. Phys. Chem. C* 121 (2017) 3194.
- [69] S.S. Fedotov, N.A. Kabanova, A.A. Kabanov, V.A. Blatov, N.R. Khasanova, E.V. Antipov, *Solid State Ionics* 314 (2018) 129.
- [70] M. Kunz, T. Armbruster, *Acta Crystallograph. Sect. B* 48 (1992) 609.
- [71] G. Ceder, M.K. Aydinol, A.F. Kohan, *Comput. Mater. Sci.* 8 (1997) 161.
- [72] A. Pedone, *J. Phys. Chem. C* 113 (2009) 20773.

Supplementary material "Understanding migration barriers for monovalent ion insertion in transition metal oxide and phosphate based cathode materials: A DFT study"

D. A. Aksyonov^a, S. S. Fedotov^{a,b}, K. J. Stevenson^a, A. Zhugayevych^a

^a*Skolkovo Institute of Science and Technology, 143026 Moscow, Russian Federation*

^b*Department of Chemistry, Lomonosov Moscow State University, 119991 Moscow, Russian Federation*

Table S1: Average intercalation potential (E) and potential required for creating alkali vacancy (E_{vac}) in fully intercalated compound and alkali interstitial cation in fully deintercalated compound relative to metallic Li using DFT calculations. All potentials are in V.

structure	E	E_{vac}	E_{int}
LiMn ₂ O ₄	3.4	2.9	-3.9
NaMn ₂ O ₄	2.4	2.0	-2.8
KMn ₂ O ₄	0.7	1.8	0.1
LiFePO ₄	3.0	2.2	-3.5
NaFePO ₄	2.6	1.8	-3.1
KFePO ₄	2.2	2.0	-1.7
LiMnPO ₄	3.0	2.9	-3.3
NaMnPO ₄	2.7	2.6	-3.0
KMnPO ₄	2.3	2.6	-1.8
LiVPO ₄ F	3.1	2.7	-3.5
NaVPO ₄ F	3.0	2.7	-3.1
KVPO ₄ F	2.5	2.5	-1.8

Table S2: Average intercalation potential (E) and potential required for creating alkali vacancy (E_{vac}) in fully intercalated compound and alkali interstitial cation in fully deintercalated compound relative to metallic Li using DFT+U calculations. All potentials are in V.

structure	E	E_{vac}	E_{int}
LiMn ₂ O ₄	3.8	3.8	-3.6
NaMn ₂ O ₄	2.9	2.8	-2.5
KMn ₂ O ₄	1.4	2.4	0.1
LiFePO ₄	3.4	3.8	-3.1
NaFePO ₄	3.1	3.4	-2.7
KFePO ₄	2.6	3.2	-1.0
LiMnPO ₄	3.8	3.9	-3.8
NaMnPO ₄	3.5	3.6	-3.4
KMnPO ₄	3.1	3.3	-2.1
LiVPO ₄ F	4.0	4.3	-4.0
NaVPO ₄ F	3.8	4.2	-3.5
KVPO ₄ F	3.4	3.7	-2.2

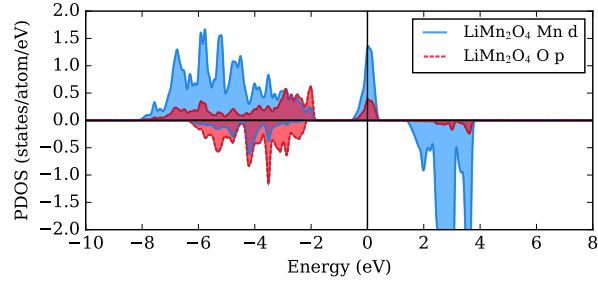


Figure S1: Site-projected PDOS for LiMn_2O_4 ($Fd\bar{3}m$)

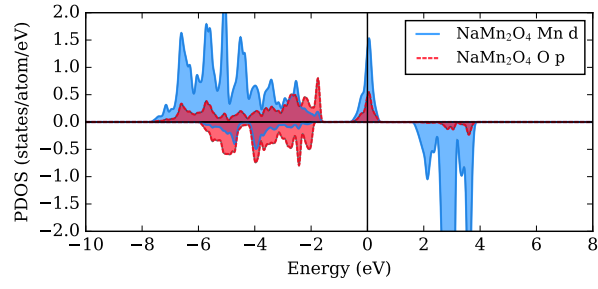


Figure S2: Site-projected PDOS for NaMn_2O_4 ($Fd\bar{3}m$)

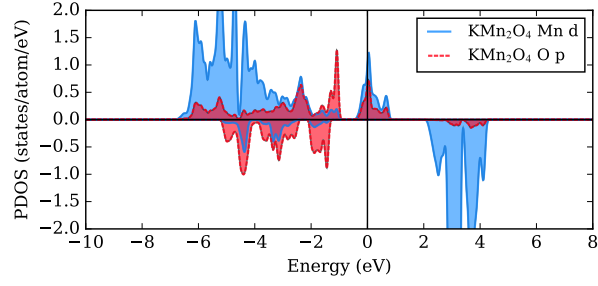


Figure S3: Site-projected PDOS for KMn_2O_4 ($Fd\bar{3}m$)

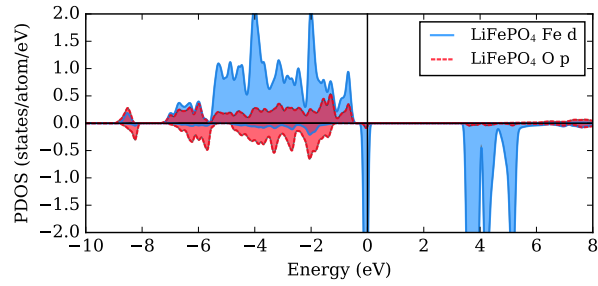


Figure S4: Site-projected PDOS for LiFePO_4 ($Pnma$)

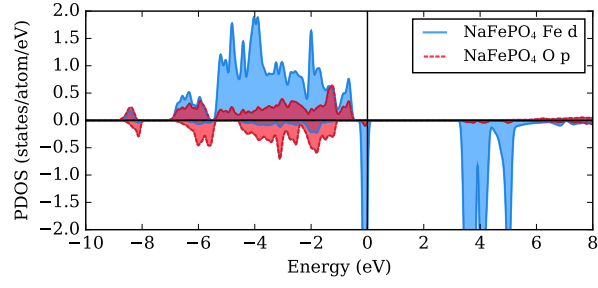


Figure S5: Site-projected PDOS for NaFePO₄ (*Pnma*)

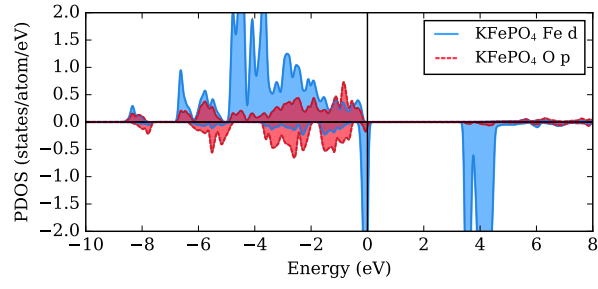


Figure S6: Site-projected PDOS for KFePO₄ (*Pnma*)

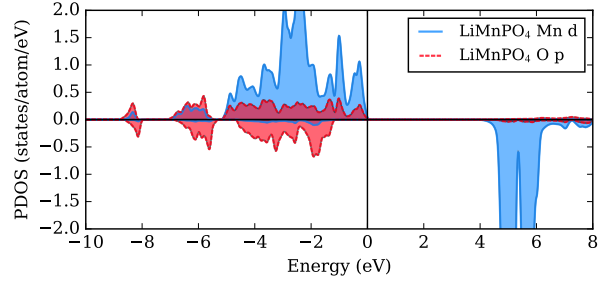


Figure S7: Site-projected PDOS for LiMnPO₄ (*Pnma*)

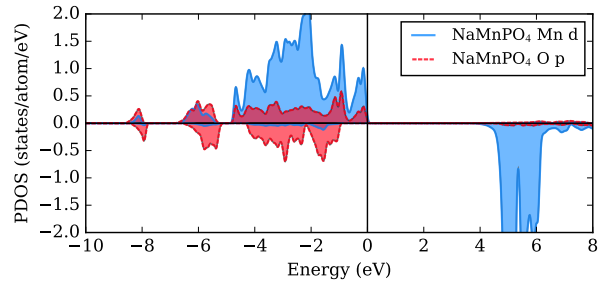


Figure S8: Site-projected PDOS for NaMnPO₄ (*Pnma*)

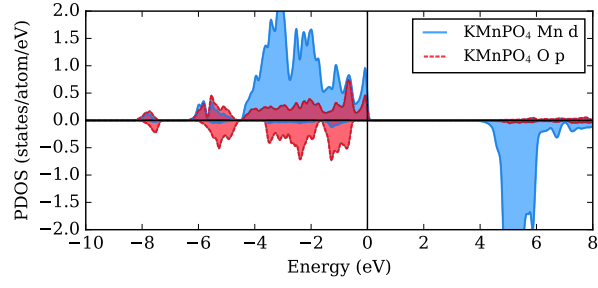


Figure S9: Site-projected PDOS for KMnPO_4 ($Pnma$)

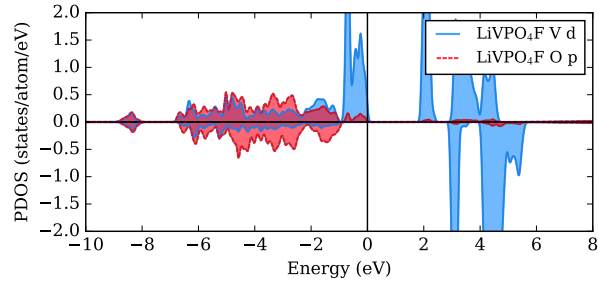


Figure S10: Site-projected PDOS for LiVPO_4F ($P\bar{1}$)

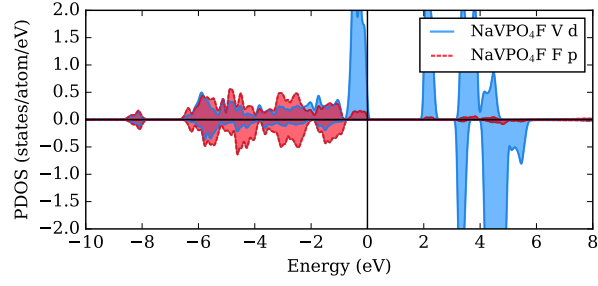


Figure S11: Site-projected PDOS for NaVPO_4F ($P\bar{1}$)

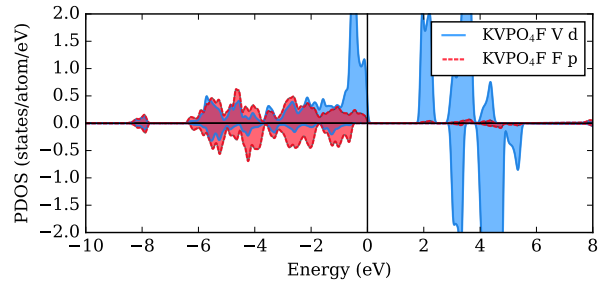


Figure S12: Site-projected PDOS for KVPO_4F ($P\bar{1}$)

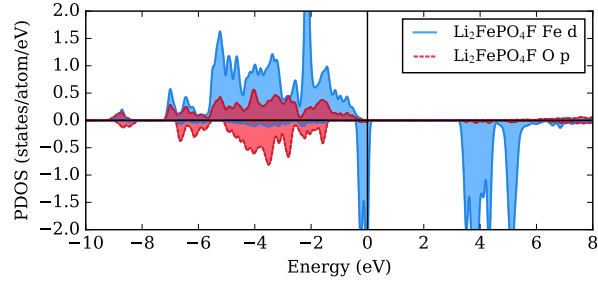


Figure S13: Site-projected PDOS for $\text{Li}_2\text{FePO}_4\text{F}$ ($Pnma$)

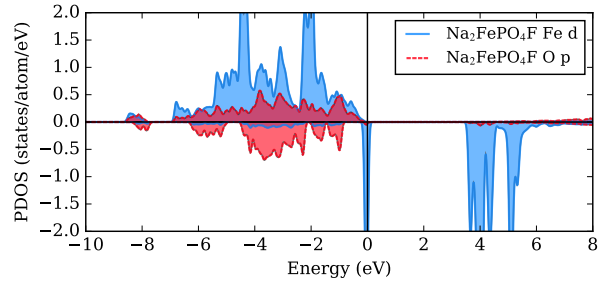


Figure S14: Site-projected PDOS for $\text{Na}_2\text{FePO}_4\text{F}$ ($Pnma$)

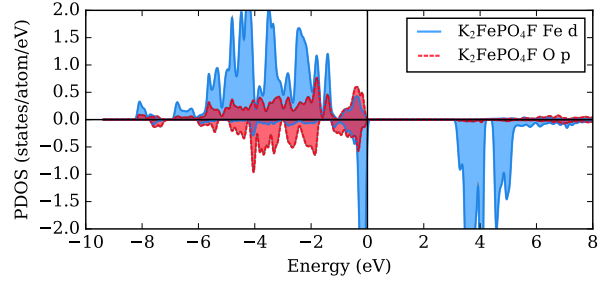


Figure S15: Site-projected PDOS for $\text{K}_2\text{FePO}_4\text{F}$ ($Pnma$)

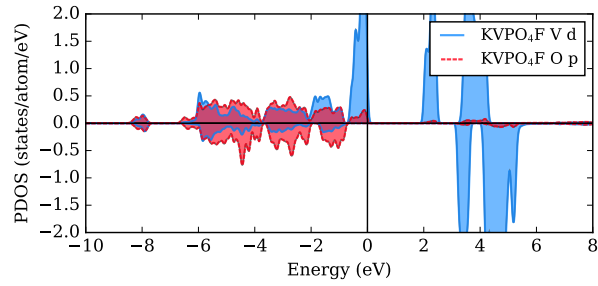


Figure S16: Site-projected PDOS for KVPO_4F ($Pna2_1$)

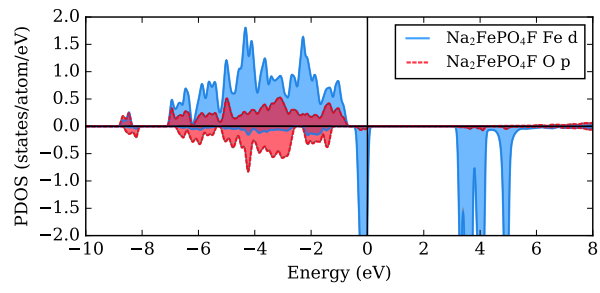


Figure S17: Site-projected PDOS for $\text{Na}_2\text{FePO}_4\text{F}$ ($Pbcn$)

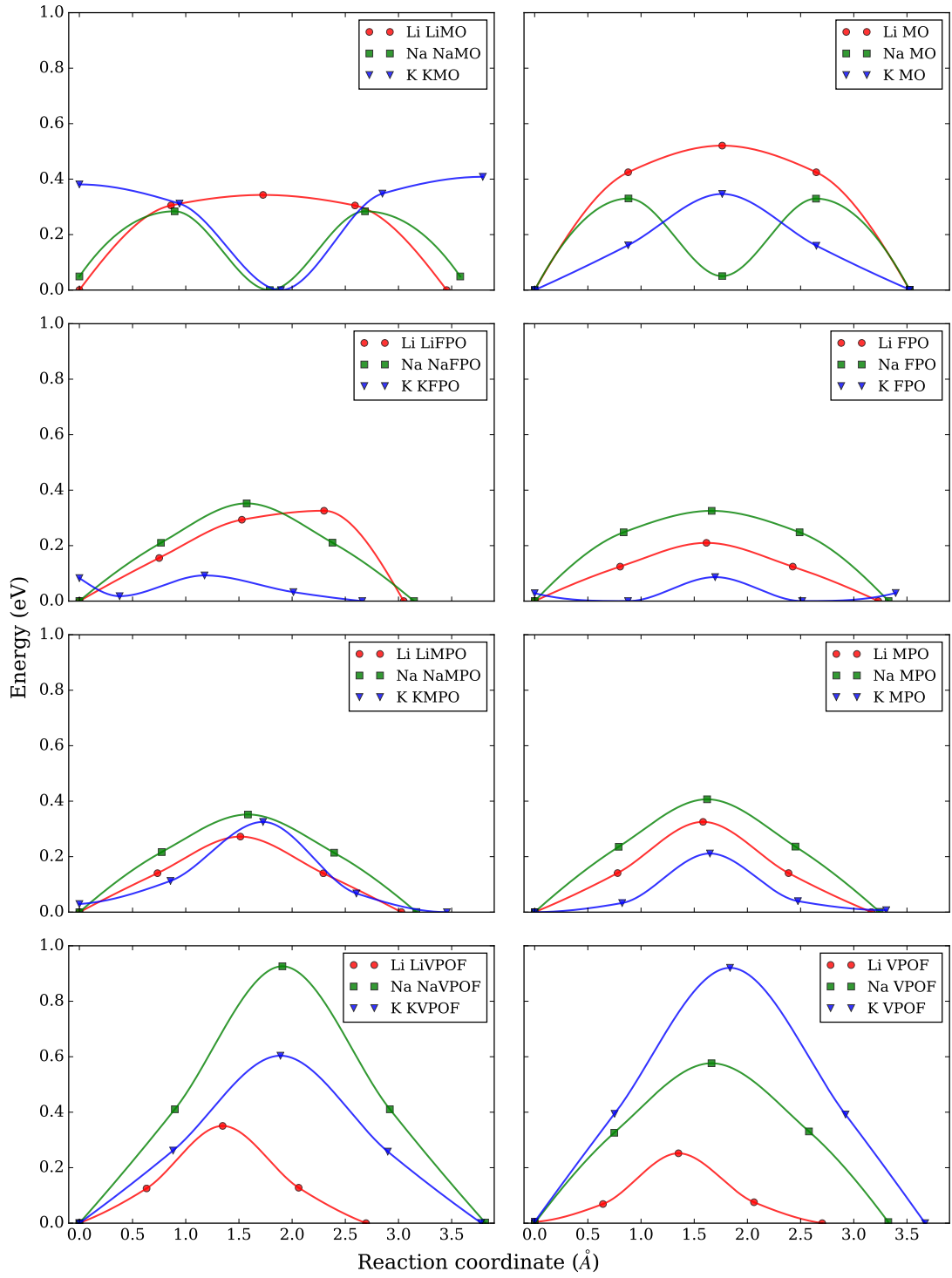


Figure S18: Energy profiles for the investigated Li-Li, Na-Na, and K-K migration pathways in fully intercalated and fully deintercalated states calculated with DFT-NEB method. MO = Mn_2O_4 , FPO = FePO_4 , MPO = MnPO_4 , VPOF = VPO_4F